Parametric and Tensor-Based Nonparametric Filtering for Extended Object Tracking with Mixed Euclidean–Directional States

Jiachen Zhou, Marvin Schanz, Noah Jens, Harald Kruggel-Emden, and Uwe D. Hanebeck

Abstract— **This paper considers recursive state estimation for two-dimensional maneuvering extended object tracking from point-cloud measurements. The system state comprises Euclidean-valued kinematic and shape variables as well as a heading angle evolving on the unit circle $\mathbb{S}^1$. In contrast to the Euclidean state components, the heading angle is intrinsically directional and periodic. Hence, it cannot be consistently modeled as an ordinary Euclidean random variable. To address the resulting mixed Euclidean–directional estimation problem, we propose and compare two filtering approaches. First, a parametric filter based on directional statistics models the joint state probability density function using a partially wrapped normal distribution. Its properties relevant to sampling-based recursive estimation are investigated, including sample generation and parameter estimation. Second, a nonparametric tensor-decomposition-based grid filter discretizes the complete state space on a regular grid while representing the high-dimensional discrete probability density tensor in decomposed form, thereby mitigating the computational burden associated with conventional full-grid filtering. Both approaches are evaluated in an extended object tracking scenario based on a coordinated-turn motion model. Estimation accuracy is compared to characterize the trade-off between structured parametric directional modeling and flexible tensor-decomposition-based nonparametric density estimation.**

Index Terms— **Bayesian inference, extended object tracking, directional statistics, tensor decomposition.**

I. INTRODUCTION

Modern spatially resolving sensing systems frequently provide multiple measurements originating from different locations of a single physical object, rather than only one centroid-related observation. In such cases, the object cannot be adequately represented as a point target, since its spatial extent contains relevant information that should be estimated jointly with its kinematics. This setting gives rise to the problem of extended object tracking (EOT), in which the dynamically evolving motion state and the object extent are recursively inferred from sets of spatially distributed measurements [1], [2]. Beyond established applications in robotics and autonomous systems, EOT is also relevant to particle measurement and sensor-based sorting, where recursively estimating particle motion and morphology from spatially resolved observations can support downstream characterization and sorting tasks [3], [4].

In this paper, we consider planar maneuvering EOT from noisy point-cloud measurements generated at an object's boundary. The object's kinematic state, heading angle, and spatial extent are recursively estimated from successive measurement sets. Unlike point-target tracking, the measurement likelihood depends jointly on the object's kinematic state, orientation, and extent. Therefore, these quantities must be inferred within a joint probabilistic estimation framework.

A central challenge is that the state is defined on a mixed Euclidean–directional space. Position, velocity, and extent variables are Euclidean, whereas the heading angle is periodic and lies on $\mathbb{S}^1$. Treating this angle as Euclidean may introduce artificial discontinuities at the angular boundary and misleading uncertainty representations. This issue is particularly relevant in EOT, where the nonlinear measurement likelihood couples uncertain orientation and spatial extent, inducing strongly non-Gaussian posterior densities.

State-of-the-art: Various approaches have been proposed for representing and recursively estimating extended-object shapes. Random-matrix-based approaches represent an elliptic extent by a positive-definite random matrix, yielding compact models for joint motion and extent estimation [5]. Random Hypersurface Models (RHMs) instead relate measurements to randomly scaled points on a shape boundary, enabling explicit estimation of elliptic and star-convex extents from spatially distributed measurements [2]. To represent more complex shapes, level-set RHMs have been introduced for nonconvex targets [6], while Gaussian-process-based contour models allow star-convex boundaries to be learned online [7]. More recently, implicit inside–out representations based on the stochastic medial axis transform have been investigated for Bayesian EOT, particularly for elongated object extents [8]. Nevertheless, when the state of a maneuvering object includes an uncertain heading angle, the probabilistic representation must additionally account for the circular structure of the orientation variable.

Directional statistics [9], [10] provides a principled basis for modeling random quantities on periodic domains. For planar orientations, distributions such as the wrapped normal and von Mises distributions [11], [12] avoid the artificial boundary effects that arise when angles are treated as unconstrained Euclidean variables. For states containing both circular and Euclidean components, the partially wrapped normal (PWN) distribution extends wrapped-normal modeling to mixed state spaces and captures angular–linear correlations within a single joint parametric density [13].

Jiachen Zhou, Marvin Schanz, and Uwe D. Hanebeck are with the Intelligent Sensor-Actuator-Systems Laboratory (ISAS), Institute for Anthropomatics and Robotics, Karlsruhe Institute of Technology (KIT), Germany (e-mail: jiachen.zhou@kit.edu; uqsnq@student.kit.edu; uwe.hanebeck@kit.edu).
Noah Jens and Harald Kruggel-Emden are with the Chair of Mechanical Process Engineering and Solids Processing, Institute of Chemical and Process Engineering, Technische Universität Berlin (TUB), Germany (e-mail: noah.jens@tu-berlin.de; kruggel-emden@tu-berlin.de).

Its hybrid moments further provide a practical basis for reconstructing the density parameters from weighted samples. This construction is well suited to the planar heading-angle representation considered here, whereas general three-dimensional orientation uncertainty evolves on $\mathrm{SO}(3)$ and is not intrinsically represented by a PWN density.

Grid-based density representations provide a flexible nonparametric alternative, as they can capture skewed or multimodal probability density functions (PDFs) without prescribing a parametric family. This flexibility is particularly relevant to maneuvering EOT, where nonlinear measurement updates may produce posterior structures that are difficult to represent compactly. Moreover, the heading dimension can be discretized periodically to respect its circular topology. However, a full discretization of the state space leads to a high-dimensional probability tensor whose storage and computational costs grow rapidly with the state dimension and grid resolution. Tensor decompositions mitigate this limitation by approximating the full tensor through low-rank factors [14]. Such representations have been employed in recursive Bayesian grid filtering for Euclidean state spaces, as introduced in [15] and subsequently extended and investigated in [16], [17]. More recently, tensor-decomposed regular-grid filtering with Fokker–Planck prediction has been extended to cylindrical manifolds by treating the angular dimension periodically in the finite-difference representation [18]. This provides a natural basis for the proposed nonparametric method for mixed Euclidean–directional EOT.

Motivation: Although directional-statistical and tensor-based representations provide principled means of handling periodic heading uncertainty, their comparative performance in point-cloud-based maneuvering EOT remains to be assessed under a common estimation task. In particular, it is of interest how the compactness of a parametric representation compares with the flexibility of a nonparametric density model when jointly estimating kinematics, heading, and spatial extent. Addressing this question is our central focus.

Contribution: We formulate and compare two recursive estimators for maneuvering Bayesian EOT on a mixed Euclidean–directional state space. The first estimator, termed the partially wrapped normal filter (PWNF), employs a PWN density to jointly represent a single heading angle and Euclidean kinematic and extent variables. Prediction and filter update are performed by sample-based recursive processing followed by hybrid-moment-based parameter reconstruction. This provides compact uncertainty representation at the cost of being restricted to the PWN family.

The second estimator, termed the tensor-decomposed grid filter (TDGF), represents the joint state density nonparametrically on a regular product grid with a periodic angular dimension. To mitigate the computational burden of full-grid filtering, the discrete probability tensor is represented in canonical polyadic decomposition (CPD) form as a weighted sum of rank-one outer products of one-dimensional loading vectors. The TDGF therefore retains the flexibility of a grid-based density representation while exploiting a separable low-rank structure for computational tractability.

Both estimators are evaluated in a coordinated-turn scenario [19], highlighting the trade-off between compact parametric and flexible nonparametric density representations.

II. Problem Formulation

Throughout this paper, scalars are written without underlining, vectors are underlined, and matrices are boldface. Random scalars and vectors are additionally written in boldface, while the corresponding realizations are written in regular font. We consider recursive estimation of a maneuvering extended object in a two-dimensional Cartesian environment from sequentially acquired point-cloud measurements. At time step k, the system state is represented by

$$\underline{\boldsymbol{x}}_k = \left[{}^{I}\underline{\boldsymbol{c}}_k^\top,\, \boldsymbol{v}_k,\, {}^{I}\boldsymbol{\varphi}_k,\, \boldsymbol{\omega}_k,\, \underline{\boldsymbol{s}}_k^\top\right]^\top , \tag{1}$$

where ${}^{I}\underline{\boldsymbol{c}}_k \in \mathbb{R}^2$ denotes the object center in the inertial frame, $\boldsymbol{v}_k$, ${}^{I}\boldsymbol{\varphi}_k$, and $\boldsymbol{\omega}_k$ denote its translational speed, heading angle, and turn rate, respectively, and $\underline{\boldsymbol{s}}_k$ contains the extent parameters. Since the heading angle is defined modulo 2π, it is naturally associated with the unit circle $\mathbb{S}^1$. Hence, the state takes values in the mixed Euclidean–directional space $\mathcal{X} = \mathbb{R}^{n_\mathrm{E}} \times \mathbb{S}^1$ of dimension $D_\mathcal{X} = n_\mathrm{E} + 1$, where n_E denotes the Euclidean component dimension. Accordingly, any state density expressed in terms of the angular coordinate ${}^{I}\varphi_k$ must be 2π-periodic in that coordinate.

At each discrete time step k, the measurement process is described by N_k random measurement vectors $\{{}^{I}\underline{\boldsymbol{y}}_{k,i} \in \mathbb{R}^2\}_{i=1}^{N_k}$. Their corresponding realizations constitute the observed point-cloud measurement set $\mathcal{Y}_k = \{{}^{I}\underline{\tilde{y}}_{k,i} \in \mathbb{R}^2\}_{i=1}^{N_k}$. In contrast to point-target tracking, the measurements are modeled as noisy observations of spatially distributed sources along the object boundary rather than of the object center alone. Let $\partial\mathcal{S}(\underline{\boldsymbol{s}}_k) \subset \mathbb{R}^2$ denote the object boundary in the body-fixed frame B, parameterized by the extent state $\underline{\boldsymbol{s}}_k$. Each measurement is associated with a latent random source point ${}^{B}\underline{\boldsymbol{z}}_{k,i} \in \partial\mathcal{S}(\underline{\boldsymbol{s}}_k)$, $i = 1, \ldots, N_k$. The corresponding source in the inertial frame is obtained by transforming the body-frame source point according to the object pose, i.e.,

$$\begin{aligned} {}^{I}\mathbf{R}_B({}^{I}\boldsymbol{\varphi}_k) &= \begin{bmatrix} \cos({}^{I}\boldsymbol{\varphi}_k) & -\sin({}^{I}\boldsymbol{\varphi}_k) \\ \sin({}^{I}\boldsymbol{\varphi}_k) & \cos({}^{I}\boldsymbol{\varphi}_k) \end{bmatrix} , \\ {}^{I}\underline{\boldsymbol{z}}_{k,i} &= {}^{I}\underline{\boldsymbol{c}}_k + {}^{I}\mathbf{R}_B({}^{I}\boldsymbol{\varphi}_k)\, {}^{B}\underline{\boldsymbol{z}}_{k,i} \, . \end{aligned} \tag{2}$$

Each random measurement vector is modeled as a noisy observation of the corresponding boundary source point

$${}^{I}\underline{\boldsymbol{y}}_{k,i} = {}^{I}\underline{\boldsymbol{z}}_{k,i} + \underline{\boldsymbol{\nu}}_{k,i} \, , \; i = 1, \ldots, N_k \, , \tag{3}$$

where the measurement noises are independently distributed as $\underline{\boldsymbol{\nu}}_{k,i} \sim \mathcal{N}(\underline{0}, \mathbf{C}^\nu)$, and $\mathbf{C}^\nu$ denotes the Cartesian measurement-noise covariance. Thus, the measurement model directly depends on the object center ${}^{I}\underline{\boldsymbol{c}}_k$, the heading angle ${}^{I}\boldsymbol{\varphi}_k$, and the extent parameters $\underline{\boldsymbol{s}}_k$. The speed $\boldsymbol{v}_k$ and turn rate $\boldsymbol{\omega}_k$ affect the measurements indirectly through the temporal evolution of the position and heading.

Between consecutive measurements, the state evolves according to the continuous-time Itô stochastic differential equation

$$\mathrm{d}\underline{\boldsymbol{x}}(t) = \underline{\psi}\big(\underline{\boldsymbol{x}}(t), t\big)\,\mathrm{d}t + \mathbf{G}\big(\underline{\boldsymbol{x}}(t), t\big)\,\mathrm{d}\underline{\boldsymbol{\beta}}(t)\,, \tag{4}$$

where $\underline{\psi}(\cdot,\cdot)$ denotes the drift vector, $\mathbf{G}(\cdot,\cdot)$ is the diffusion matrix, and $\underline{\boldsymbol{\beta}}(t)$ is a Brownian motion process satisfying $\mathbb{E}\big\{\mathrm{d}\underline{\boldsymbol{\beta}}(t)\,\mathrm{d}\underline{\boldsymbol{\beta}}^\top(t)\big\} = \mathbf{Q}(t)\,\mathrm{d}t$. The angular component of (4) is interpreted modulo 2π. Alternatively, a discrete-time state model is given by

$$\underline{\boldsymbol{x}}_k = \underline{a}_k(\underline{\boldsymbol{x}}_{k-1}) + \underline{\boldsymbol{w}}_k\,, \tag{5}$$

where $\underline{\boldsymbol{w}}_k$ denotes the system noise.

Recursive Bayesian estimation propagates and updates the state PDF over time. The posterior density after incorporating the measurement sets $\mathcal{Y}_{1:k} = \{\mathcal{Y}_1, \ldots, \mathcal{Y}_k\}$ is denoted by

$$f^{\mathrm{e}}_{\underline{\boldsymbol{x}}_k}(\underline{x}_k) = f_{\underline{\boldsymbol{x}}_k}(\underline{x}_k \mid \mathcal{Y}_1, \ldots, \mathcal{Y}_k) = f_{\underline{\boldsymbol{x}}_k}(\underline{x}_k \mid \mathcal{Y}_{1:k})\,, \tag{6}$$

whereas the predicted density before incorporating $\mathcal{Y}_k$ is

$$f^{\mathrm{p}}_{\underline{\boldsymbol{x}}_k}(\underline{x}_k) = f_{\underline{\boldsymbol{x}}_k}\left(\underline{x}_k \mid \mathcal{Y}_{1:k-1}\right)\,. \tag{7}$$

Each filtering cycle consists of a prediction step $f^{\mathrm{e}}_{k-1} \to f^{\mathrm{p}}_k$ followed by a measurement update $f^{\mathrm{p}}_k \to f^{\mathrm{e}}_k$.

Under (4), the state density evolves according to the Fokker–Planck equation (FPE)

$$\begin{aligned}\frac{\partial f_{\underline{\boldsymbol{x}}}(\underline{x}, t)}{\partial t} &= \mathcal{L} f_{\underline{\boldsymbol{x}}}(\underline{x}, t)\\ &= -\sum\nolimits_{i=1}^{D_{\mathcal{X}}} \frac{\partial}{\partial x_i}\big(\psi_i(\underline{x}, t) f_{\underline{\boldsymbol{x}}}(\underline{x}, t)\big)\\ &\quad + \frac{1}{2}\sum\nolimits_{i,j=1}^{D_{\mathcal{X}}} \frac{\partial^2}{\partial x_i \partial x_j}\Big(\big[\mathbf{D}(\underline{x}, t)\big]_{i,j}\, f_{\underline{\boldsymbol{x}}}(\underline{x}, t)\Big)\,, \end{aligned} \tag{8}$$

$$\mathbf{D}(\underline{x}, t) = \mathbf{G}(\underline{x}, t)\,\mathbf{Q}(t)\,\mathbf{G}^\top(\underline{x}, t)\,. \tag{9}$$

Here, $\mathcal{L}$ denotes the Fokker–Planck operator acting on the state density, and $\mathbf{D}(\underline{x}, t)$ is the diffusion tensor defined in (9). For the circular component, periodic boundary conditions are imposed. Integration over two consecutive measurement instants yields the predicted density $f^{\mathrm{p}}_{\underline{\boldsymbol{x}}_k}$ from $f^{\mathrm{e}}_{\underline{\boldsymbol{x}}_{k-1}}$.

For the discrete-time system model (5), prediction follows from the Chapman–Kolmogorov equation

$$f^{\mathrm{p}}_{\underline{\boldsymbol{x}}_k}(\underline{x}_k) = \int_{\mathcal{X}} f^{\mathrm{a}}_{\underline{\boldsymbol{x}}_k}(\underline{x}_k \mid \underline{x}_{k-1}) f^{\mathrm{e}}_{\underline{\boldsymbol{x}}_{k-1}}(\underline{x}_{k-1})\,\mathrm{d}\underline{x}_{k-1}\,. \tag{10}$$

Under the standard conditional-independence assumption, Bayes' rule gives

$$f^{\mathrm{e}}_{\underline{\boldsymbol{x}}_k}(\underline{x}_k) \propto f\left(\mathcal{Y}_k \mid \underline{x}_k\right)\, f^{\mathrm{p}}_{\underline{\boldsymbol{x}}_k}(\underline{x}_k)\,. \tag{11}$$

Assuming conditionally independent measurements,

$$f\left(\mathcal{Y}_k \mid \underline{x}_k\right) = \prod\nolimits_{i=1}^{N_k} f_{\underline{\boldsymbol{y}}_k}\big({}^{I}\underline{\tilde{y}}_{k,i} \mid \underline{x}_k\big)\,. \tag{12}$$

For later use, define the individual likelihood contribution as

$$f^{\mathrm{L}}_{k,i}(\underline{x}_k) \coloneqq f_{\underline{\boldsymbol{y}}_k}\big({}^{I}\underline{\tilde{y}}_{k,i} \mid \underline{x}_k\big)\,, \tag{13}$$

Once this likelihood function $f^{\mathrm{L}}_{k,i}(\underline{x}_k)$ is explicitly obtained, it can be incorporated into a recursive Bayesian filter.

III. Key Ideas and Groundwork

This section summarizes the two density representations underlying the estimators considered in this work: the parametric PWN distribution for mixed Euclidean–directional states and a tensor-decomposed grid representation for non-parametric density approximation.

A. The Partially Wrapped Normal Distribution

The PWN distribution represents mixed circular–linear random vectors by wrapping selected dimensions of an underlying multivariate normal distribution modulo 2π [13]. Let $\underline{\boldsymbol{\zeta}} = [\underline{\boldsymbol{\vartheta}}^\top, \underline{\boldsymbol{\ell}}^\top]^\top \in (\mathbb{S}^1)^m \times \mathbb{R}^{n-m}$, where, for notational convenience, the m circular components are placed first in this PWN coordinate representation. Its density is

$$f^{\mathrm{PWN}}_{\underline{\boldsymbol{\zeta}}}(\underline{\zeta};\, \underline{\mu},\, \mathbf{C}) = \sum\nolimits_{\underline{q}\in\mathbb{Z}^m} \mathcal{N}\big(\underline{\zeta} + [2\pi\underline{q},\, \underline{0}]^\top;\, \underline{\mu},\, \mathbf{C}\big)\,, \tag{14}$$

where $\underline{\mu}$ and $\mathbf{C}$ denote the location and covariance parameters of the underlying Gaussian representation. The parameters are partitioned according to the circular and linear components as

$$\underline{\mu} = \begin{bmatrix}\underline{\mu}_\vartheta\\ \underline{\mu}_\ell\end{bmatrix}\,, \quad \mathbf{C} = \begin{bmatrix}\mathbf{C}_{\vartheta\vartheta} & \mathbf{C}_{\vartheta\ell}\\ \mathbf{C}_{\vartheta\ell}^\top & \mathbf{C}_{\ell\ell}\end{bmatrix}\,. \tag{15}$$

Due to wrapping, $\underline{\mu}$ and $\mathbf{C}$ are generally not the Euclidean mean and covariance of $\underline{\boldsymbol{\zeta}}$. Nevertheless, $\underline{\mu}_\vartheta$ and $\mathbf{C}_{\vartheta\vartheta}$ parameterize the wrapped-normal marginal, $\underline{\mu}_\ell$ and $\mathbf{C}_{\ell\ell}$ the Gaussian marginal, and $\mathbf{C}_{\vartheta\ell}$ their circular–linear dependence.

Dirac-mixture representation: Let $\{(\underline{u}^{(r)}, w^{(r)})\}_{r=1}^{N_\mathrm{s}}$ be a Dirac-mixture approximation of $\mathcal{N}(\underline{\mu}, \mathbf{C})$, with $w^{(r)} \geq 0$ and $\sum_{r=1}^{N_\mathrm{s}} w^{(r)} = 1$. The corresponding PWN support points are obtained by wrapping only the circular coordinates of $\underline{u}^{(r)}$ modulo 2π,

$$\underline{s}^{(r)} = \Big[\big(\operatorname{wrap}_{2\pi}(\underline{u}_\vartheta^{(r)})\big)^\top,\, \big(\underline{u}_\ell^{(r)}\big)^\top\Big]^\top\,, \tag{16}$$

while retaining the weights $w^{(r)}$.

Hybrid moments: For the single circular component considered here, direct Euclidean moments are inappropriate because the angular representation is periodic. In particular, angles near 0 and 2π represent similar directions but are far apart in their scalar representation. We therefore employ a sine–cosine embedding, which removes this artificial discontinuity before moment matching. Given weighted PWN samples $\underline{s}^{(r)} = [s_\vartheta^{(r)},\, (\underline{s}_\ell^{(r)})^\top]^\top$, $r = 1, \ldots, N_\mathrm{s}$, the hybrid embedding is defined as

$$\underline{\tilde{s}}^{(r)} = \big[\cos(s_\vartheta^{(r)}),\, \sin(s_\vartheta^{(r)}),\, (\underline{s}_\ell^{(r)})^\top\big]^\top\,. \tag{17}$$

The corresponding weighted hybrid moments are

$$\underline{\tilde{\mu}} = [\tilde{\mu}_{\cos}\,,\, \tilde{\mu}_{\sin}\,,\, \underline{\tilde{\mu}}_\ell^\top]^\top = \sum\nolimits_{r=1}^{N_\mathrm{s}} w^{(r)}\, \underline{\tilde{s}}^{(r)}\,, \tag{18}$$

$$\tilde{\mathbf{C}} = \sum\nolimits_{r=1}^{N_\mathrm{s}} w^{(r)} (\underline{\tilde{s}}^{(r)} - \underline{\tilde{\mu}})\, (\underline{\tilde{s}}^{(r)} - \underline{\tilde{\mu}})^\top\,. \tag{19}$$

The pair $(\tilde{\mu}_{\cos}, \tilde{\mu}_{\sin})$ determines the mean direction and mean resultant length of the circular component, while the remaining moments characterize the linear components and their dependence on the heading.

Parameter estimation: For a single circular component, the PWN parameters are obtained by hybrid-moment matching [13, Sec. III-D]. With $\overline{R} = \sqrt{\tilde{\mu}_{\cos}^2 + \tilde{\mu}_{\sin}^2}$, the circular location and uncertainty parameter are estimated as

$$\hat{\mu}_\vartheta = \mathrm{wrap}_{2\pi}\left(\mathrm{atan2}(\tilde{\mu}_{\sin}, \tilde{\mu}_{\cos})\right),\ \hat{c}_{\vartheta\vartheta} = -2\log(\overline{R}). \quad (20)$$

The linear mean and covariance block are directly matched as $\hat{\underline{\mu}}_\ell = \tilde{\underline{\mu}}_\ell$ and $\hat{\mathbf{C}}_{\ell\ell} = \tilde{\mathbf{C}}_{\ell\ell}$, whereas the circular–linear correlation cross block $\hat{\mathbf{C}}_{\vartheta\ell}$ is reconstructed according to

$$\hat{\mathbf{C}}_{\vartheta\ell} = \exp(\hat{c}_{\vartheta\vartheta}/2)\big(-\sin(\hat{\mu}_\vartheta)\,\tilde{\mathbf{C}}_{\cos,\ell} + \cos(\hat{\mu}_\vartheta)\,\tilde{\mathbf{C}}_{\sin,\ell}\big)\,.$$

Thus, the reconstructed uncertainty parameter is

$$\hat{\mathbf{C}} = \begin{bmatrix} \hat{c}_{\vartheta\vartheta} & \hat{\mathbf{C}}_{\vartheta\ell} \\ \hat{\mathbf{C}}_{\vartheta\ell}^\top & \hat{\mathbf{C}}_{\ell\ell} \end{bmatrix}. \quad (21)$$

Here, $\tilde{\mathbf{C}}_{\cos,\ell}$ and $\tilde{\mathbf{C}}_{\sin,\ell}$ denote the covariance blocks between the embedded circular and the linear components.

B. Tensor-Decomposed Grid Representation

Unlike the parametric PWN model, a grid representation approximates the state density non-parametrically and can therefore capture non-Gaussian and multimodal distributions.

Regular grid design: Each Euclidean component x_d is restricted to a bounded interval $[\xi_d^{\min}, \xi_d^{\max}]$ and discretized by N_d equidistant nodes, whereas the heading angle is discretized on an endpoint-exclusive periodic grid with N_φ nodes. The resulting discrete state PDF is stored as a $D_{\mathcal{X}}$-way tensor $\mathfrak{P} \in \mathbb{R}^{N_1 \times \cdots \times N_{n_\mathrm{E}} \times N_\varphi}$. The endpoint-exclusive angular grid avoids duplicating the equivalent angles 0 and 2π and supports periodic finite-difference operators. Normalization and moment evaluation use the corresponding product-grid quadrature weights.

Curse of dimensionality: The flexibility of the regular-grid representation comes at the cost of exponential storage and computational complexity. The full tensor contains $N_1 \times \cdots \times N_{n_\mathrm{E}} \times N_\varphi$ entries, which reduces to $\mathcal{O}(N^{D_{\mathcal{X}}})$ for a uniform grid with N nodes per dimension. Hence, direct full-grid filtering is computationally demanding for the joint kinematic–extent state considered here [16], [17].

Kronecker-structured operators: Efficient density propagation on high-dimensional product grids requires avoiding the explicit construction of prohibitively large full-space evolution operators. For notational simplicity, assume N grid nodes per state dimension and define the vectorized grid density as $\underline{p} := \mathrm{vec}(\mathfrak{P}) \in \mathbb{R}^{N^{D_{\mathcal{X}}}}$. The discretized density evolution is given by

$$\frac{\mathrm{d}}{\mathrm{d}t}\,\underline{p}(t) = \mathbf{L}\,\underline{p}(t)\,, \quad \mathbf{L} \in \mathbb{R}^{N^{D_{\mathcal{X}}} \times N^{D_{\mathcal{X}}}}\,. \quad (22)$$

If the underlying coefficient functions are separable or replaced by a low-rank separable approximation, the resulting discretized operator can be written as a sum of Kronecker products,

$$\mathbf{L} = \sum\nolimits_{\ell=1}^{M_{\mathcal{L}}} \bigotimes\nolimits_{d=1}^{D_{\mathcal{X}}} \mathbf{A}_d^{(\ell)}\,, \quad \mathbf{A}_d^{(\ell)} \in \mathbb{R}^{N \times N}\,. \quad (23)$$

Here, $M_{\mathcal{L}}$ denotes the number of separable terms, and $\mathbf{A}_d^{(\ell)}$ is a one-dimensional differentiation, multiplication, or identity operator acting along dimension d. This structure enables the action of $\mathbf{L}$ to be evaluated through one-dimensional factors without assembling the full-space matrix.

While the Kronecker structure in (23) enables efficient evolution operator application, the full density tensor $\mathfrak{P}$ still suffers from exponential storage cost. Therefore, $\mathfrak{P}$ is approximated in CPD format [14], [20]. Under the uniform node-count notation, the $D_{\mathcal{X}}$-way tensor is represented as a weighted sum of rank-one outer products,

$$\mathfrak{P} \approx \sum\nolimits_{r=1}^{R} \lambda_r\, \underline{\rho}_{1,r} \circ \underline{\rho}_{2,r} \circ \cdots \circ \underline{\rho}_{D_{\mathcal{X}},r}\,, \quad \underline{\rho}_{d,r} \in \mathbb{R}^N\,, \quad (24)$$

where R is the decomposition rank, λ_r is the r-th rank-one component weight, and $\underline{\rho}_{d,r}$ denotes the loading vector in the d-th dimension. Equivalently, after vectorization,

$$\underline{p} = \mathrm{vec}(\mathfrak{P}) \approx \sum\nolimits_{r=1}^{R} \lambda_r \bigotimes\nolimits_{d=1}^{D_{\mathcal{X}}} \underline{\rho}_{d,r}\,. \quad (25)$$

Although each rank-one term is separable, their weighted sum can capture dependencies across state dimensions. Hence, CPD does not enforce mutual independence unless only a single rank-one component is retained.

Structured operator application: The CPD format is particularly compatible with the Kronecker operator representation in (23). Inserting (25) into the action of $\mathbf{L}$ yields

$$\mathbf{L}\,\underline{p} \approx \sum\nolimits_{\ell=1}^{M_{\mathcal{L}}} \sum\nolimits_{r=1}^{R} \lambda_r \bigotimes\nolimits_{d=1}^{D_{\mathcal{X}}} \big(\mathbf{A}_d^{(\ell)}\,\underline{\rho}_{d,r}\big)\,. \quad (26)$$

Thus, each separable operator acts only on one-dimensional loading vectors, avoiding the construction of the full tensor and full-space matrix. Since these operations may increase the decomposition rank during propagation, rank reduction [21] is applied to maintain tractability.

Storage complexity: Under the uniform N-node assumption, a rank-R CPD representation requires $\mathcal{O}(RD_{\mathcal{X}}N)$ parameters plus R component weights, compared with $\mathcal{O}(N^{D_{\mathcal{X}}})$ entries for the full tensor. For moderate R, the storage scaling is therefore reduced from exponential in the state dimension $D_{\mathcal{X}}$ to linear in both $D_{\mathcal{X}}$ and N.

IV. Recursive Estimation for the Polar Coordinated-Turn Model

This section specializes the two estimators, PWNF and TDGF, to an elliptic extended object with polar coordinated-turn kinematics [19]. The state is defined in (1), and the extent is parameterized by logarithmic semi-axis variables $\underline{\boldsymbol{s}}_k = [\boldsymbol{s}_k^a,\ \boldsymbol{s}_k^b]^\top$. The physical semi-axis lengths are given by $\boldsymbol{a}_k^\mathrm{E} = \exp(\boldsymbol{s}_k^a)$ and $\boldsymbol{b}_k^\mathrm{E} = \exp(\boldsymbol{s}_k^b)$. This exponential mapping $\exp(\cdot)$ guarantees positive semi-axis lengths while keeping the extent state unconstrained.

A. Polar CT Motion Model and Ellipse Likelihood

Both estimators share the coordinated-turn kinematics but use different prediction representations. The PWNF propagates samples with the discrete-time model (5), whereas the TDGF propagates the density through the continuous-time Fokker–Planck model (8). For the PWNF, the polar coordinated-turn model is applied to the kinematic state $[{}^I\underline{\boldsymbol{c}}_k^\top,\ \boldsymbol{v}_k,\ {}^I\boldsymbol{\varphi}_k,\ \boldsymbol{\omega}_k]^\top$. Let $\underline{f}_\mathrm{p}$ denote the nominal transition for zero longitudinal and angular acceleration and $\mathbf{G}_{\mathrm{p}}^2({}^I\varphi)$ the corresponding zero-order-hold input matrix [19, Eq. (4), (5)]. Including the constant extent parameters yields

$$\underline{\boldsymbol{x}}_k = \underline{g}(\underline{\boldsymbol{x}}_{k-1}) + \tilde{\mathbf{G}}_{\mathrm{p}}^2({}^I\varphi_{k-1})\,\underline{\boldsymbol{w}}_k\,, \tag{27}$$

with

$$\underline{g}(\underline{x}) = \begin{bmatrix} \underline{f}_{\mathrm{p}}({}^I\underline{c}, v, {}^I\varphi, \omega) \\ \underline{s} \end{bmatrix}\,,\ \tilde{\mathbf{G}}_{\mathrm{p}}^2({}^I\varphi) = \begin{bmatrix} \mathbf{G}_{\mathrm{p}}^2({}^I\varphi) \\ \mathbf{0}_{2\times 2} \end{bmatrix}\,. \tag{28}$$

The process-noise input is

$$\underline{\boldsymbol{w}}_k = [\tilde{\boldsymbol{a}}_k,\, \tilde{\boldsymbol{\alpha}}_k]^\top \sim \mathcal{N}\big(\underline{0},\, \mathrm{diag}(\sigma_{\tilde{a}}^2,\, \sigma_{\tilde{\alpha}}^2)\big)\,, \tag{29}$$

where $\tilde{\boldsymbol{a}}_k$ and $\tilde{\boldsymbol{\alpha}}_k$ are piecewise-constant longitudinal and angular acceleration inputs over the sampling interval Δt. Their one-step contributions satisfy $\mathrm{Var}(\Delta v) = \sigma_{\tilde{a}}^2 \Delta t^2$ and $\mathrm{Var}(\Delta\omega) = \sigma_{\tilde{\alpha}}^2 \Delta t^2$.

For the TDGF, a continuous-time white-noise acceleration model with the same nominal coordinated-turn kinematics is employed. With zero deterministic acceleration input, the drift vector in (4) is

$$\underline{\psi}\big(\underline{x}(t), t\big) = \big[v\cos({}^I\varphi)\,, v\sin({}^I\varphi)\,, 0\,, \omega\,, 0\,, \underline{0}_2^\top\big]^\top\,. \tag{30}$$

Process uncertainty acts in the v- and ω-directions, with

$$\mathbf{G} = \begin{bmatrix} 0 & 0 & 1 & 0 & 0 & \underline{0}_2^\top \\ 0 & 0 & 0 & 0 & 1 & \underline{0}_2^\top \end{bmatrix}^\top\,,\ \mathbf{Q} = \begin{bmatrix} \sigma_a^2 & 0 \\ 0 & \sigma_\alpha^2 \end{bmatrix}\,. \tag{31}$$

To match the one-step process uncertainty of the discrete-time model in the directly driven states v and ω, the diffusion parameters are chosen as

$$\sigma_a^2 = \sigma_{\tilde{a}}^2 \Delta t\,, \quad \sigma_\alpha^2 = \sigma_{\tilde{\alpha}}^2 \Delta t\,. \tag{32}$$

Together with (30), these matrices define the Fokker–Planck prediction model used by the TDGF.

The measurement likelihood is formulated using the Spatial Distribution Model (SDM) [22, Eq. (10)], where the unknown association between a measurement and its generating boundary point is described probabilistically. A source parameter is drawn according to a spatial distribution on the object boundary, and the corresponding boundary point is then corrupted by additive Gaussian measurement noise. Thus, the source parameter acts as a nuisance variable that is marginalized in the likelihood. For an elliptic extent, a boundary point in the body-fixed frame is parameterized by

$${}^B\underline{z}(\theta,\, \underline{s}_k) = \big[a_k^{\mathrm{E}}\cos(\theta),\, b_k^{\mathrm{E}}\sin(\theta)\big]^\top\,, \quad \theta \in [0,\, 2\pi)\,. \tag{33}$$

The corresponding point in the inertial frame is

$${}^I\underline{h}(\underline{x}_k,\, \theta) = {}^I\underline{c}_k + {}^I\mathbf{R}_B({}^I\varphi_k)\, {}^B\underline{z}(\theta,\, \underline{s}_k)\,. \tag{34}$$

The likelihood of an individual measurement ${}^I\underline{\tilde{y}}_{k,i}$ is obtained by marginalizing the unknown source parameter θ,

$$f_{k,i}^{\mathrm{L}}(\underline{x}_k) = \int_0^{2\pi} \mathcal{N}\big({}^I\underline{\tilde{y}}_{k,i};\, {}^I\underline{h}(\underline{x}_k,\, \theta), \mathbf{C}^\nu\big)\, f(\theta \mid \underline{x}_k)\, \mathrm{d}\theta. \tag{35}$$

Here, $\mathbf{C}^\nu$ denotes the measurement noise covariance. In this work, the source parameter is assumed to be uniformly distributed on $[0, 2\pi)$, i.e., $f(\theta \mid \underline{x}_k) = 1/(2\pi)$.

B. Application of the Partially Wrapped Normal Filter

The PWNF represents predicted, posterior, and intermediate densities in the PWN coordinate convention introduced in Sec. III-A. At time step $k-1$, the posterior density is therefore approximated as

$$f_{\underline{\boldsymbol{x}}_{k-1}}^{\mathrm{e}}(\underline{x}_{k-1}) \approx f_{\underline{\boldsymbol{x}}}^{\mathrm{PWN}}(\underline{x}_{k-1};\, \underline{\hat{\mu}}_{k-1}^{\mathrm{e}},\, \hat{\mathbf{C}}_{k-1}^{\mathrm{e}})\,. \tag{36}$$

For prediction, a weighted support-point approximation is generated from this PWN density and propagated through the discrete-time transition model in (27), including the process-noise input. The angular component is wrapped modulo 2π after propagation, and the predicted PWN parameters $(\underline{\hat{\mu}}_k^{\mathrm{p}}, \hat{\mathbf{C}}_k^{\mathrm{p}})$ are reconstructed from the propagated support points by hybrid-moment matching.

The measurement update is performed progressively [23], [24] to avoid incorporating the complete measurement-set likelihood at once. For a progression parameter $\gamma \in [0, 1]$, we define the progressive likelihood function

$$f^\gamma\left(\mathcal{Y}_k \mid \underline{x}_k\right) = \prod\nolimits_{i=1}^{N_k} \left[f_{k,i}^{\mathrm{L}}(\underline{x}_k)\right]^\gamma\,. \tag{37}$$

Following [23, Eq. (10)], the update from γ to $\gamma + \Delta\gamma$ is realized by applying the incremental likelihood factor $f^{\Delta\gamma}(\mathcal{Y}_k \mid \underline{x}_k)$. At each progression step, equal-weight deterministic samples are generated from the current PWN approximation by applying deterministic Gaussian sampling [25] to the underlying normal distribution and wrapping the circular component. The sample weights are then multiplied by the incremental likelihood $f^{\Delta\gamma}(\mathcal{Y}_k \mid \underline{x}_k)$. The step size $\Delta\gamma$ is chosen such that the ratio between the smallest and largest nonzero updated weights remains above a threshold τ, analogous to [24, Sec. IV-C]. After normalization, a new PWN density is fitted by hybrid-moment matching. This procedure is repeated until $\gamma = 1$. Thus, the update can be interpreted as a mixed circular–linear version of progressive Gaussian filtering [23], where the intermediate posterior approximations are represented by PWNs.

C. Application of the Tensor-Decomposed Grid Filter

The TDGF represents the state density on the regular product grid introduced in Sec. III-B. The posterior density tensor at $k-1$ is stored in the CPD form of (24)

$$\mathfrak{P}_{k-1}^{\mathrm{e}} \approx \sum\nolimits_{r=1}^{R} {}^{\mathrm{r}}\lambda_{k-1}^{\mathrm{e}}\, {}^{\mathrm{r}}\underline{\rho}_{1,k-1}^{\mathrm{e}} \circ \cdots \circ {}^{\mathrm{r}}\underline{\rho}_{D_{\mathcal{X}},k-1}^{\mathrm{e}}\,. \tag{38}$$

Under the rigid-shape assumption, the shape parameters have zero drift and diffusion during Fokker–Planck prediction. Hence, the continuous FPE in (8) reduces to

$$\begin{aligned} \frac{\partial f_{\underline{\boldsymbol{x}}}(\underline{x}, t)}{\partial t} &= -v\cos({}^I\varphi)\frac{\partial f_{\underline{\boldsymbol{x}}}}{\partial {}^I c_x} - v\sin({}^I\varphi)\frac{\partial f_{\underline{\boldsymbol{x}}}}{\partial {}^I c_y} - \omega\frac{\partial f_{\underline{\boldsymbol{x}}}}{\partial {}^I\varphi} \\ &\quad + \frac{\sigma_a^2}{2}\frac{\partial^2 f_{\underline{\boldsymbol{x}}}}{\partial v^2} + \frac{\sigma_\alpha^2}{2}\frac{\partial^2 f_{\underline{\boldsymbol{x}}}}{\partial \omega^2}\,. \end{aligned} \tag{39}$$

For the present coordinated-turn model, the Fokker–Planck operator admits an exact finite separable representation because the drift coefficients $v\cos({}^I\varphi)$ and $v\sin({}^I\varphi)$ factor into products of one-dimensional functions, while the remaining transport coefficient ω depends on a single state dimension and the diffusion coefficients are state independent. For example, the term $-v\cos({}^{I}\varphi)\,\partial f_{\underline{x}}/\partial^{I}c_x$ is represented by a first-derivative finite-difference matrix in the ${}^{I}c_x$ dimension, diagonal multiplication matrices for v and $\cos({}^{I}\varphi)$ in their respective dimensions, and identity matrices in all remaining dimensions. The remaining transport and diffusion terms are constructed analogously. Periodic finite differences [18, Eq. (10)] are used for the heading dimension, while non-periodic finite differences are used on the truncated Euclidean domains. After finite-difference discretization, the operator $\mathbf{L}$ takes the Kronecker-structured form (23). Its separable terms correspond to transport in ${}^{I}c_x$, ${}^{I}c_y$, and ${}^{I}\varphi$, and diffusion in v and ω. The one-dimensional factors consist of finite-difference matrices and diagonal multiplication matrices containing the grid values of v, ω, $\cos({}^{I}\varphi)$, and $\sin({}^{I}\varphi)$. Periodic finite differences [18, Eq. (10)] are used for the heading dimension, while non-periodic finite differences are used on the truncated Euclidean domains.

Formally, prediction over one interval Δt is given by the matrix-exponential density propagation [16, Eq. (13)] $\underline{p}_k^{\mathrm{p}} = \exp(\Delta t\,\mathbf{L})\,\underline{p}_{k-1}^{\mathrm{e}}$. Following the Kronecker-product approximation strategy of [16, Eq. (17)], neither the full operator $\mathbf{L}$ nor the full matrix exponential is explicitly formed. Instead, the separable operator terms in (23) are applied directly to the 1D CPD factors using a Taylor approximation with N_{sub} temporal substeps of length $\tau = \Delta t/N_{\mathrm{sub}}$. Since each Taylor contribution remains separable but increases the intermediate CP rank, rank pruning and final CPD compression are applied to obtain the predicted low-rank density tensor $\mathfrak{P}_k^{\mathrm{p}}$.

For the measurement update, the TDGF applies (11) on the product grid. Since the ellipse likelihood depends directly only on position, heading, and extent, it is evaluated on the subgrid $({}^{I}c_x, {}^{I}c_y, {}^{I}\varphi, s^a, s^b)$ and extended to the full state grid by unit factors in the v- and ω-dimensions. This yields a CPD approximation $\mathfrak{L}_k$ of the likelihood in (12) without redundant evaluations in unobserved dimensions.

The pointwise Bayesian update is then given by $\mathfrak{P}_k^{\mathrm{e}} \propto \mathfrak{P}_k^{\mathrm{p}} \odot \mathfrak{L}_k$ where $\odot$ denotes elementwise multiplication. In CPD form, this multiplication is realized by pairwise products of component weights and elementwise products of the corresponding loading vectors. This procedure increases the intermediate CPD rank. After normalization with the product-grid quadrature weights, the posterior tensor is compressed back to the prescribed CPD rank to control rank growth and obtain $\mathfrak{P}_k^{\mathrm{e}}$.

V. Evaluation

We evaluate the proposed filters in the planar maneuvering EOT scenario described in Sec. IV using 30 independent Monte Carlo runs. Fig. 1 illustrates one representative run. Positions and semi-axis lengths are measured in m, speed in $\mathrm{m/s}$, heading in rad, and turn rate in $\mathrm{rad/s}$. The logarithmic extent variables are unit-free length ratios, with $s^a = \log(a^{\mathrm{E}}/1\,\mathrm{m})$ and $s^b = \log(b^{\mathrm{E}}/1\,\mathrm{m})$.

The ground-truth trajectory starts from

$$\underline{x}_0 = [0,\ 0,\ 10,\ \pi/6,\ 0.05\pi,\ \log(15),\ \log(6)]^\top . \tag{40}$$

The logarithmic extent entries correspond to physical semi-axis lengths of $15\,\mathrm{m}$ and $6\,\mathrm{m}$, normalized by the reference length $1\,\mathrm{m}$. To assess convergence under a biased initialization, each filter is initialized with an imperfect prior mean

$$\hat{\underline{x}}_0 = [15,\ -15,\ 10,\ \pi/5,\ 0.05\pi,\ \log(10),\ \log(10)]^\top . \tag{41}$$

The stochastic coordinated-turn model of Sec. IV is used with $\sigma_{\tilde{a}} = 0.5\,\mathrm{m/s^2}$ and $\sigma_{\tilde{\alpha}} = 0.15\,\mathrm{rad/s^2}$. The PWNF employs the discrete-time model in (27), whereas the TDGF uses the corresponding continuous-time drift and diffusion model in (30) and (31). Each run comprises $K = 200$ time steps with a sampling period of $\Delta t = 0.2\,\mathrm{s}$. At each step, 50 noisy measurements are generated from spatially distributed source points on the elliptic boundary according to (3). The measurement noise is isotropic with standard deviation $\sigma_\nu = 2\,\mathrm{m}$ in each Cartesian coordinate, i.e., $\mathbf{C}^\nu = \sigma_\nu^2\,\mathbf{I}_2 = 4\,\mathrm{m}^2\,\mathbf{I}_2$. Complete target visibility is assumed, without clutter, false detections, or missed detections.

The TDGF employs a regular product grid of $80\times80\times10\times72\times10\times20\times20$ nodes for $({}^{I}c_x,\ {}^{I}c_y,\ v,\ {}^{I}\varphi,\ \omega,\ s^a,\ s^b)$. Its initial density is represented by an independent rank-one CPD, formed from one-dimensional Gaussian marginals for the Euclidean state components and a wrapped Gaussian marginal for the heading angle. Fokker–Planck prediction uses a third-order Taylor approximation of the matrix-exponential action with $N_{\mathrm{sub}} = 2$ temporal substeps, followed by compression to the nominal target rank $R = 8$.

Estimation accuracy is evaluated using the time-dependent Root Mean Square Error (RMSE) for each state component over all Monte Carlo runs. For the heading, the error is computed as a wrapped angular difference to avoid artificial discontinuities at the 2π boundary,

$$e_{\varphi,k}^{(m)} = \operatorname{atan2}\left(\sin(\hat{\varphi}_k^{(m)} - \varphi_k^{(m)}),\ \cos(\hat{\varphi}_k^{(m)} - \varphi_k^{(m)})\right) . \tag{42}$$

We include the Multiplicative Error Model (MEM)-Extended Kalman Filter (EKF)* as a state-of-the-art baseline. It represents orientation as part of the shape state and propagates the corresponding covariance [26, Eq. (2)]. Using the multiplicative-error measurement model [26, Eq. (5)], it updates the kinematic state directly from the measurements and

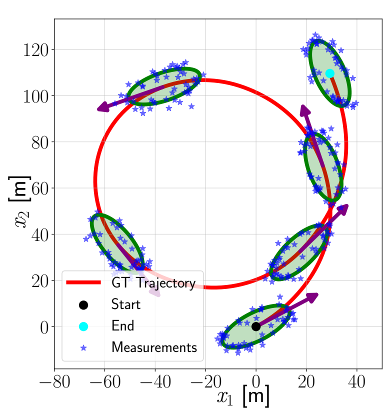

Fig. 1: Ground-truth trajectory and measurements for one representative Monte Carlo run over 200 time steps.

TABLE I: Recorded computational cost of the proposed filters. Time/step denotes the mean recorded wall-clock processing time per complete recursion step of one trajectory, averaged over 30 independent Monte Carlo runs with $K = 200$.

Method	Time/step [s]	Relative time
PWNF	0.286 ± 0.029	$1.0\times$
TDGF	13.128 ± 0.679	$45.9\times$

the shape state from pseudo-measurements based on second-order residuals [26, Eq. (24)]. Its Gaussian formulation treats the orientation angle as a Euclidean scalar. We further include a Euclidean Unscented Kalman Filter (UKF) using the same state vector and likelihood model as the PWNF. It models all state components jointly by a Gaussian density without wrapping or circular moments, thereby serving as a baseline for assessing the effect of ignoring angular periodicity.

Fig. 2 shows the kinematic-state RMSE over time for the different filtering methods. The UKF rapidly diverges because it treats angular states as Euclidean random variables and therefore neglects their circular nature. Both proposed methods remain stable, but show different characteristics. The PWNF exhibits noticeable fluctuations in the position and heading-angle estimates, whereas the TDGF converges more stably and yields smaller errors in these components. In particular, the TDGF clearly outperforms the MEM-EKF* in heading-angle estimation.

Fig. 3 shows the corresponding RMSE results for the estimated shape parameters. The logarithmic shape variables are first transformed to the physical semi-axis lengths a^{E} and b^{E}, and the RMSE is computed in meters. For both semi-axis parameters, the TDGF quickly converges to very small errors and remains stable throughout the evaluation interval. Compared with the MEM-EKF*, the TDGF substantially reduces the shape-estimation error.

Table I compares the recorded computational cost of the two proposed filters. The compact parametric PWNF is approximately 46 times faster than the nonparametric TDGF in the recorded implementations. This illustrates the computational cost associated with the more flexible product-grid density representation of the TDGF.

Table II compares the nominal configuration with lower- and higher-rank variants as well as coarser and finer grids. Each configuration uses 4 Monte Carlo runs with $K = 50$ time steps and 50 measurements per step. Increasing the rank beyond $R = 8$ yields only marginal changes, while finer grids improve most metrics at substantially higher computational cost. Although the retained CPD storage increases linearly with the target rank for a fixed grid, the measured runtime is not monotonic in this experiment. The runtime depends not only on the retained rank but also on the convergence behavior of the iterative CPD compression routine. Therefore, the observed timing differences should not be interpreted as evidence that a higher target rank is generally computationally cheaper.

VI. Conclusion

We compared the parametric PWNF and nonparametric TDGF for maneuvering EOT with mixed Euclidean–directional states. The two approaches represent different trade-offs between compact parametric modeling and flexible nonparametric density representation. The results highlight the importance of respecting angular periodicity. The TDGF provides more stable position and heading estimates than the PWNF and improves heading and shape estimation over the considered MEM-EKF* baseline.

The present evaluation is limited to controlled simulations with complete target visibility and clutter-free boundary measurements. Extending the measurement model to account for partial visibility, occlusions, clutter, false detections, and missed detections is important for future work.

VII. Acknowledgments

The IGF project 01IF22901N of the research association Forschungs-Gesellschaft Verfahrenstechnik e.V. (GVT) is supported in a program to promote Industrial Collective Research (IGF) by the Federal Ministry for Economic Affairs and Energy on the basis of a resolution of the German Bundestag.

References

[1] Karl Granstrom, Marcus Baum, and Stephan Reuter. “Extended object tracking: Introduction, overview and applications”. In: *arXiv preprint arXiv:1604.00970* (2016).

[2] Marcus Baum and Uwe D. Hanebeck. “Extended Object Tracking with Random Hypersurface Models”. In: *IEEE Transactions on Aerospace and Electronic Systems* 50 (Jan. 2014), pp. 149–159. DOI: 10.1109/TAES.2013.120107.

[3] Georg Maier, Florian Pfaff, Matthias Wagner, Christoph Pieper, Robin Gruna, Benjamin Noack, Harald Kruggel-Emden, Thomas Längle, Uwe D Hanebeck, Siegmar Wirtz, et al. “Real-time multitarget tracking for sensor-based sorting: A new implementation of the auction algorithm for graphics processing units”. In: *Journal of Real-Time Image Processing* 16.6 (2019), pp. 2261–2272.

[4] Georg Maier, Florian Pfaff, Florian Becker, Christoph Pieper, Robin Gruna, Benjamin Noack, Harald Kruggel-Emden, Thomas Längle, Uwe D Hanebeck, Siegmar Wirtz, et al. “Motion-based material characterization in sensor-based sorting”. In: *tm-Technisches Messen* 85.3 (2018), pp. 202–210.

[5] Johann Wolfgang Koch. “Bayesian approach to extended object and cluster tracking using random matrices”. In: *IEEE Transactions on Aerospace and Electronic Systems* 44.3 (2008), pp. 1042–1059.

[6] Antonio Zea, Florian Faion, Marcus Baum, and Uwe D. Hanebeck. “Level-Set Random Hypersurface Models for Tracking Nonconvex Extended Objects”. In: *IEEE Transactions on Aerospace and Electronic Systems* (2016). DOI: 10.1109/TAES.2016.130704.

[7] Niklas Wahlström and Emre Özkan. “Extended target tracking using Gaussian processes”. In: *IEEE Transactions on Signal Processing* 63.16 (2015), pp. 4165–4178.

[8] Jiachen Zhou, Uwe D. Hanebeck, Albert Bauer, and Harald Kruggel-Emden. “Stochastic Medial Axis Transform for Bayesian Extended Object Tracking”. In: *Proceedings of the 28th International Conference on Information Fusion (FUSION 2025)*. Rio de Janeiro, Brazil, July 2025. DOI: 10.23919/FUSION65864.2025.11124170.

[9] Kanti V Mardia and Peter E Jupp. *Directional statistics*. John Wiley & Sons, 2009.

[10] Nicholas I Fisher. *Statistical analysis of circular data*. cambridge university press, 1995.

[11] Gerhard Kurz, Igor Gilitschenski, and Uwe D. Hanebeck. “Recursive Nonlinear Filtering for Angular Data Based on Circular Distributions”. In: *Proceedings of the 2013 American Control Conference (ACC 2013)*. Washington D.C., USA, June 2013. DOI: 10.1109/acc.2013.6580688.

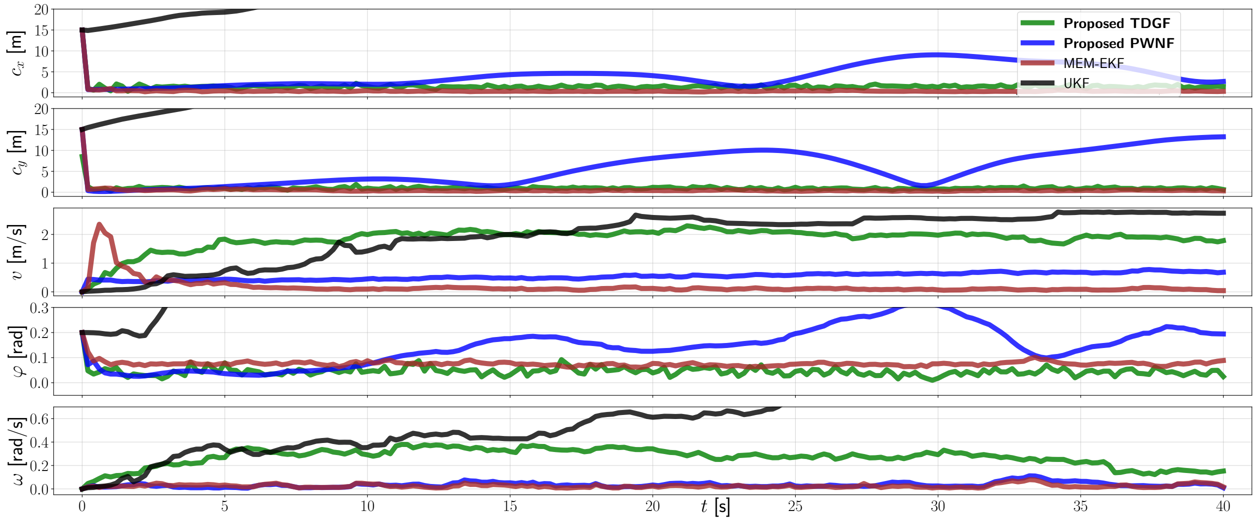

Fig. 2: Kinematic-state RMSE over time for different filtering methods. At each time step, the RMSE is computed over all independent Monte Carlo runs.

TABLE II: TDGF numerical sensitivity and computational cost. Runtime is the mean per-trajectory filtering time per step. Grid entries are $(N_x, N_y, N_\varphi, N_a, N_b)$. $N_v = N_\omega = 10$ in all cases.

Case	Grid	R	Pos. RMSE [m] ↓	Head. RMSE [°] ↓	a RMSE [m] ↓	b RMSE [m] ↓	Time/step [s] ↓
Low rank	80/80/72/20/20	4	1.610	2.922	**0.359**	0.277	13.422
Nominal	80/80/72/20/20	8	1.529	**2.742**	**0.359**	0.232	11.416
High rank	80/80/72/20/20	12	**1.509**	2.839	**0.359**	**0.224**	**10.870**
Coarse grid	60/60/48/15/15	8	2.052	3.857	0.616	0.256	**3.236**
Fine grid	100/100/96/25/25	8	**1.232**	**2.644**	**0.572**	**0.063**	29.614

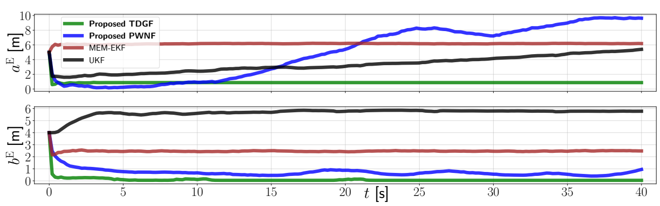

Fig. 3: Time-dependent RMSE in m of the physical semi-axis lengths over all Monte Carlo runs. Logarithmic shape estimates are mapped to lengths via $a^{\mathrm{E}} = \ell_0 \exp(s^a)$ and $b^{\mathrm{E}} = \ell_0 \exp(s^b)$ with $\ell_0 = 1\,\mathrm{m}$.

[12] Gerhard Kurz, Igor Gilitschenski, and Uwe D. Hanebeck. "Recursive Bayesian Filtering in Circular State Spaces". In: *IEEE Aerospace and Electronic Systems Magazine* 31.3 (Mar. 2016), pp. 70–87. DOI: 10.1109/MAES.2016.150083.

[13] Gerhard Kurz, Igor Gilitschenski, and Uwe D. Hanebeck. "The Partially Wrapped Normal Distribution for SE(2) Estimation". In: *Proceedings of the 2014 IEEE International Conference on Multisensor Fusion and Information Integration (MFI 2014)*. Beijing, China, Sept. 2014. DOI: 10.1109/MFI.2014.6997733.

[14] Frank L Hitchcock. "The expression of a tensor or a polyadic as a sum of products". In: *Journal of Mathematics and Physics* 6.1-4 (1927), pp. 164–189.

[15] Yifei Sun and Mrinal Kumar. "Nonlinear Bayesian filtering based on Fokker-Planck equation and tensor decomposition". In: *2015 18th International Conference on Information Fusion (Fusion)*. IEEE. 2015, pp. 1483–1488.

[16] Bruno Demissie, Muhammad Altamash Khan, and Felix Govaers. "Nonlinear filter design using Fokker-Planck propagator in Kronecker tensor format". In: *2016 19th International Conference on Information Fusion (FUSION)*. IEEE. 2016, pp. 1–8.

[17] Felix Govaers, Bruno Demissie, Altamash Khan, Martin Ulmke, and Wolfgang Koch. "Tensor decomposition-based multitarget tracking in cluttered environments". In: *Journal of advances in information fusion* 14.1 (2019), p. 86.

[18] Daniel Frisch and Uwe D. Hanebeck. "Fokker-Planck Prediction on the Cylindric Manifold using Tensor Decomposition of a Regular Grid". In: *17th Symposium Sensor Data Fusion: Trends, Solutions, Applications (SDF 2025)*. Bonn, Germany, Nov. 2025. DOI: 10.1109/SDF67080.2025.11330240.

[19] Michael Roth, Gustaf Hendeby, and Fredrik Gustafsson. "EKF/UKF maneuvering target tracking using coordinated turn models with polar/Cartesian velocity". In: *17th International Conference on Information Fusion (FUSION)*. IEEE. 2014, pp. 1–8.

[20] Tamara G Kolda and Brett W Bader. "Tensor decompositions and applications". In: *SIAM review* 51.3 (2009), pp. 455–500.

[21] Gregory Beylkin and Martin J Mohlenkamp. "Algorithms for numerical analysis in high dimensions". In: *SIAM Journal on Scientific Computing* 26.6 (2005), pp. 2133–2159.

[22] Florian Faion, Antonio Zea, Marcus Baum, and Uwe D. Hanebeck. "Partial Likelihood for Unbiased Extended Object Tracking". In: *Proceedings of the 18th International Conference on Information Fusion (Fusion 2015)*. Washington D.C., USA, July 2015.

[23] Jannik Steinbring and Uwe D. Hanebeck. "Progressive Gaussian Filtering Using Explicit Likelihoods". In: *Proceedings of the 17th International Conference on Information Fusion (Fusion 2014)*. Salamanca, Spain, July 2014.

[24] Gerhard Kurz, Igor Gilitschenski, and Uwe D. Hanebeck. "Nonlinear Measurement Update for Estimation of Angular Systems Based on Circular Distributions". In: *Proceedings of the 2014 American Control Conference (ACC 2014)*. Portland, Oregon, USA, June 2014. DOI: 10.1109/ACC.2014.6858982.

[25] Daniel Frisch and Uwe D. Hanebeck. "Deterministic Gaussian Sampling With Generalized Fibonacci Grids". In: *Proceedings of the 24th International Conference on Information Fusion (Fusion 2021)*. Sun City, South Africa, Nov. 2021. DOI: 10.23919/FUSION49465.2021.9626975.

[26] Shishan Yang and Marcus Baum. "Tracking the orientation and axes lengths of an elliptical extended object". In: *IEEE Transactions on Signal Processing* 67.18 (2019), pp. 4720–4729.